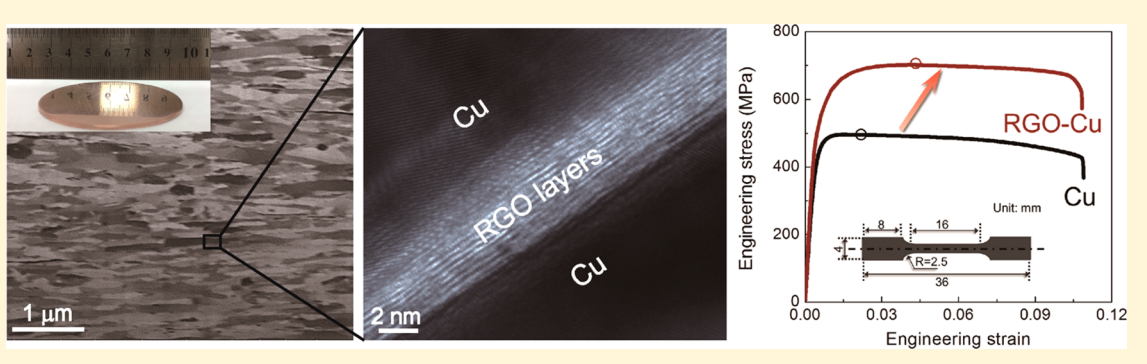
Regain Strain-Hardening in High-Strength Metals by Nanofiller **Incorporation at Grain Boundaries**

Zan Li,^{†,||} Haotian Wang,^{‡,||} Qiang Guo,^{*,†} Zhiqiang Li,[†] Ding-Bang Xiong,[†] Yishi Su,[†] Huajian Gao,[§] Xiaoyan Li,^{*,‡} and Di Zhang^{*,†}

Supporting Information

Downloaded via BROWN UNIV on May 17, 2019 at 02:48:33 (UTC). See https://pubs.acs.org/sharingguidelines for options on how to legitimately share published articles.



ABSTRACT: Grain refinement to the nano/ultrafine-grained regime can make metals several times stronger, but this process is usually accompanied by a dramatic loss of ductility. Such strength-ductility trade-off originates from a lack of strain-hardening capacity in tiny grains. Here, we present a strategy to regain the strain-hardening ability of high-strength metals by incorporation of extrinsic nanofillers at grain boundaries. We demonstrate that the dislocation storage ability in Cu grains can be considerably improved through this novel grain-boundary engineering approach, leading to a remarkably enhanced strain-hardening capacity and tensile ductility (uniform elongation). Experiments and large-scale atomistic simulations reveal that a key benefit of incorporated nanofillers is a reduction in the grain-boundary energy, enabling concurrent dislocation storage near the boundaries and in the Cu grain interior during straining. The strategy of grain-boundary engineering through nanofillers is easily controllable, generally applicable, and may open new avenues for producing nanostructured metals with extraordinary mechanical properties.

KEYWORDS: Nanostructured metals, mechanical property, grain-boundary engineering, metal matrix composites, graphene

rain boundaries can block the movement of dislocations. The yield strength of polycrystalline metals scaling inversely with the square root of the grain size, generally known as the Hall-Petch relation, was first discovered in lowcarbon steels and has since become the tenet of the strengthscaling law for metals and alloys. 1-3 For example, the strength of Cu with nanometer-sized grains can be an order of magnitude higher than that of its coarse-grained counterparts,⁴ and aluminum alloys with a grain size of tens of nanometers can achieve yield strengths greater than 1 GPa, surpassing the strength of normal steels and titanium alloys.

However, the incorporation of a large number of grain boundaries into the crystal lattice is a "double-edged sword" for the mechanical properties of metals. Grain boundaries are generally incoherent, and they consist of local disordered transition zones spanning several atomic planes between adjacent grains, giving rise to an excess of free energy compared to a crystal lattice with perfect registry. 6-8 The

excess grain-boundary energy not only makes the grain boundaries less stable but also can promote the dynamic recovery of lattice defects (e.g., point defects and dislocations) during plastic deformation. This mechanism is particularly enhanced in metals with nano/ultrafine-sized grains due to their considerable volume fraction of grain-boundary regions. In fact, grain boundaries have been convincingly demonstrated to serve as dislocation sinks in nano/ultrafine-grained metals by *in situ* tensile experiments⁹ and by computer simulations.¹⁰ Efficient dislocation annihilations at high-energy grain boundaries and a lack of dislocation storage in the grain interiors in nano/ultrafine-grained metals result in rapid exhaustion of strain-hardening abilities, leading to localized

Received: June 12, 2018 Revised: August 22, 2018 Published: September 7, 2018

[†]State Key Laboratory of Metal Matrix Composites, Shanghai Jiao Tong University, Shanghai 200240, China

[‡]Center for Advanced Mechanics and Materials, Applied Mechanics Laboratory, Department of Engineering Mechanics, Tsinghua University, Beijing 100084, China

[§]School of Engineering, Brown University, Providence, Rhode Island 02912, United States

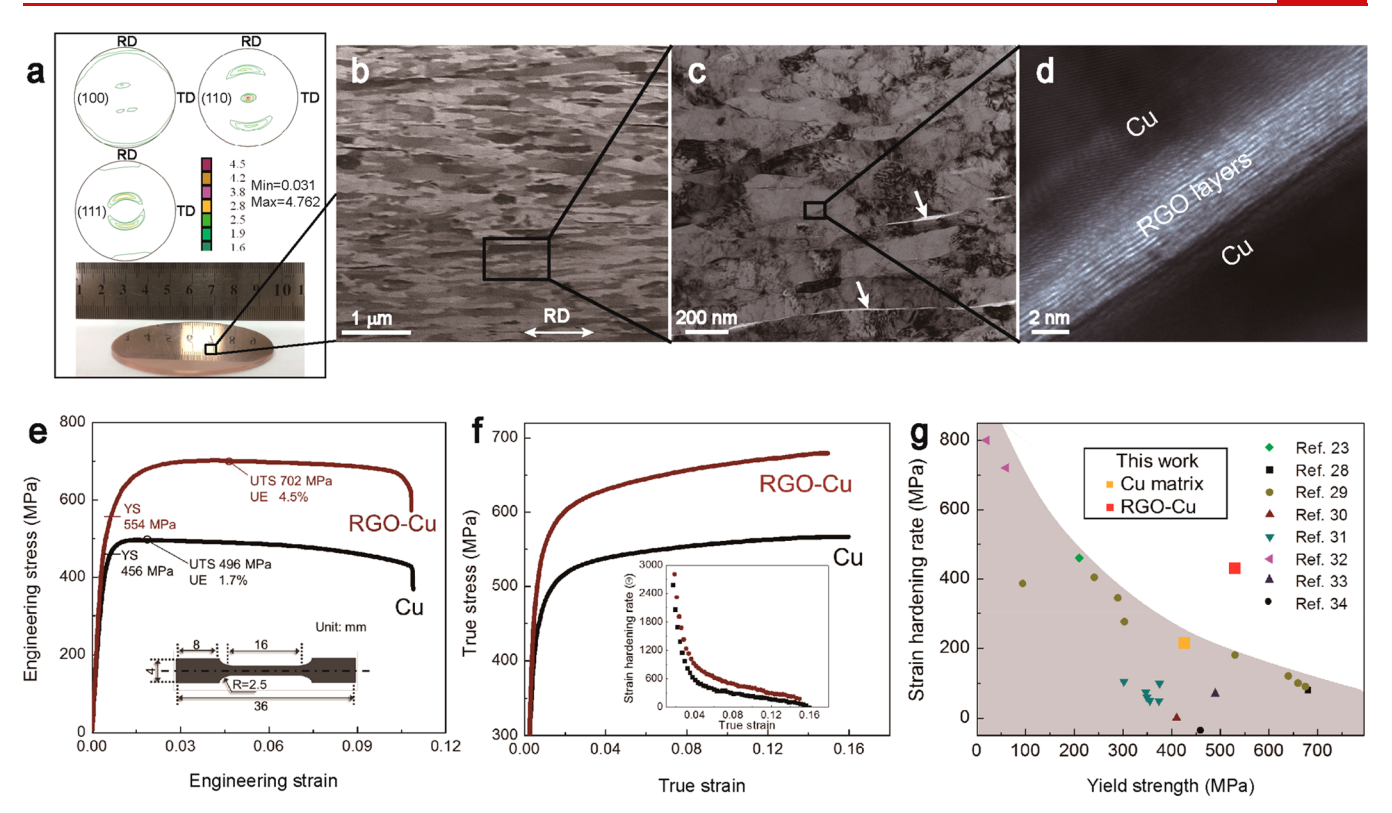


Figure 1. Typical microstructures and mechanical properties of the RGO-Cu composite. (a) Digital image of the RGO-Cu bulk composite and its pole-figure maps constructed from the XRD analysis results. (b) Cross-section FIB ion-channeling image of the RGO-Cu composite. The rolling direction (RD) is indicated by a white double-headed arrow. (c) Bright-field cross-sectional TEM image of the RGO-Cu composite. The bright areas indicated by white arrows are thicker RGO nanosheets rather than pores. (d) High-resolution TEM image taken at the boundary region of the composite. (e,) mechanical behaviors of the pure Cu matrix and the RGO-Cu composite, respectively, at a strain rate of $1 \times 10^{-3} \text{ s}^{-1}$. In particular, (e) presents representative tensile engineering stress—strain curves. The yield strength (YS), uniform elongation (UE), and ultimate tensile strength (UTS) are marked. (f) Representative compressive true stress—strain curves for the two sample sets. The maximum true strain was set to be \sim 0.16. Inset shows the strain-hardening rate (Θ)-true strain curves. (g) Summary of the compressive yield strength versus strain-hardening rate (taken from the 0.05 to 0.1 strain range) based on the data reported in this work and for pure Cu processed by various methods. $^{23,28-34}$

strain and reduced ductility, ^{11,12} as evidenced by the general observation that the tensile uniform elongation is very limited for metals with a grain size smaller than 100 nm. ¹³ Such strength—ductility trade-off has become an "Achilles' heel" for nano/ultrafine-grained metals, hindering their use in practical structural applications.

The past decade has witnessed significant progress in increasing the ductility of high-strength metals. A major consideration is to introduce low-energy internal boundaries, such as twin boundaries and low-angle grain boundaries, into the metal. 14-16 These low-energy boundaries can impede dislocation motion following a Hall-Petch type strengthening mechanism while simultaneously enabling dislocation storage through dislocation accumulations or interactions at the boundaries, 14,15 leading to improved strain-hardening ability without sacrificing high strength. The new frontier of making ductile high-strength metals is thus relying on the incorporation of internal boundaries that have the ability to hinder dislocation motion with less excess boundary energy. Although this strategy has been successfully applied in copper, 14 nickel, 15 and stainless steel¹⁶ to achieve a better balance between strength and ductility, it suffers from a strong dependence on intrinsic properties (e.g., the stacking fault energy¹⁷ and the types of precipitate phases that can be formed at the boundary⁵) of the specific metals studied and particular fabrication processes, which limits the versatility of these strategies. Therefore, a more universal method to realize grainboundary energy manipulation is greatly needed and will widen the development of high strength/ductility metals to a larger extent

In this work, we present a new approach to overcome strength-ductility trade-off in nanostructured metals by introducing a nanoscaled extrinsic reinforcing phase, referred to as "nanofillers," with at least one dimension less than 100 nm, into the grain boundaries to form a metal matrix composite. In these composites, the large lattice mismatch between the reinforcement and the matrix drives the nanofillers to migrate from the grain interiors and segregate along the grain boundaries. 18 The nature of the abundant reinforcement/metal interfaces can be elaborately tuned by tailoring the type, configuration, defect state, and concentration of the reinforcement, 19,20 affording additional freedom in designing or tuning boundaries with desired properties. Here, using nanostructured Cu reinforced with reduced graphene oxide nanosheets (RGO) as a model material, we show that the dislocation storage ability of Cu grains can be greatly enhanced by RGO incorporation at the grain boundaries, resulting in a remarkably elevated strain-hardening capacity and a profound increase in tensile ductility (uniform elongation). A combination of experimental measurements and large-scale atomistic simulations revealed that the improvements in strain-hardening capacity and tensile ductility are attributable to the substantially reduced grain-boundary energy

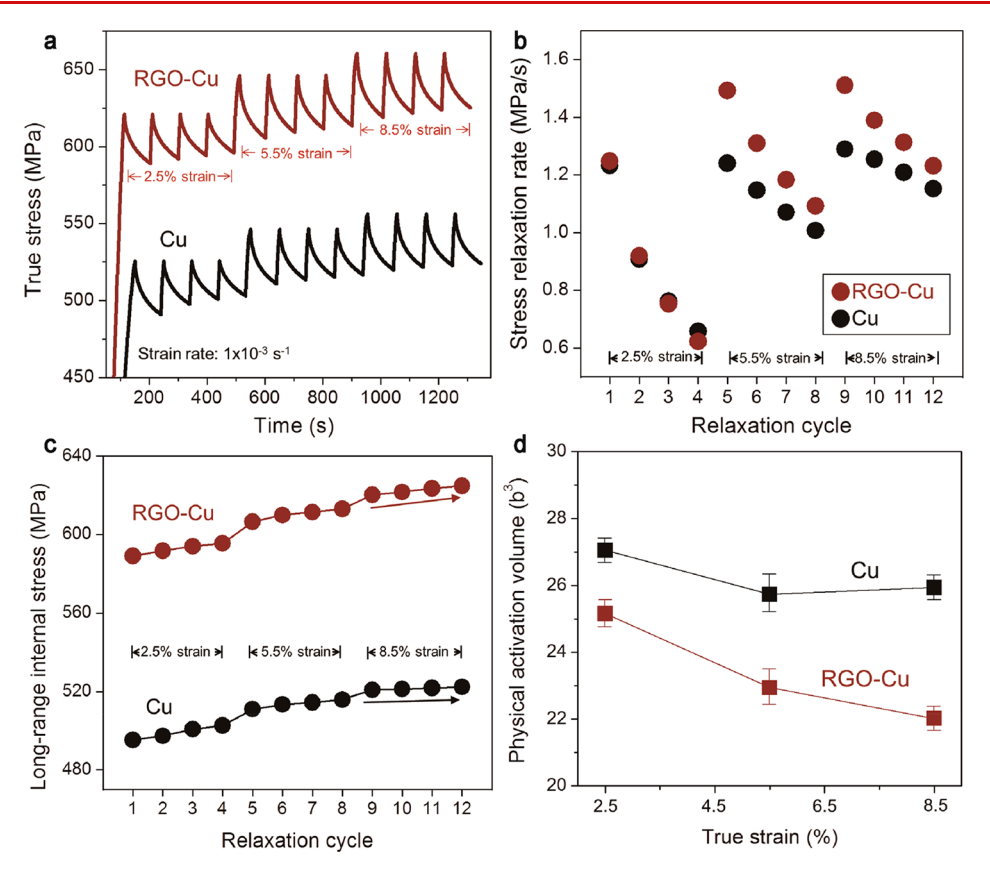


Figure 2. Progressive stress—relaxation data and extrapolated kinematic parameters obtained for the pure Cu matrix and the RGO-Cu composite. (a) Progressive multiple stress-relaxation curves for the two materials at various starting compressive true strains (2.5%, 5.5% and 8.5%). (b) Stress-relaxation rate at the onset of the holding stage for each (1st through 12th) relaxation cycle (black points for the pure Cu matrix and red points for the RGO-Cu composite). (c) Evolution of the long-range internal stress (σ_{μ}) of the pure Cu matrix and the RGO-Cu composite as a function of the number of relaxation cycles. Notably, at a true strain of 8.5%, σ_{μ} still increases with increasing relaxation cycle number for the RGO-Cu composite; however, σ_{μ} becomes almost saturated for the pure Cu matrix relaxed at a true strain of 8.5%. (d) Evolution of physical activation volume with strain for the pure Cu matrix and the RGO-Cu composite.

and the ensuing retardation of dynamic recovery of dislocations at the boundaries.

Fabricating nanofiller-reinforced metal-matrix composites with uniformly dispersed nanofillers and avoiding agglomeration-caused premature failure of the composites during straining have been challenging.²¹ To this end, we used a modified powder metallurgy approach to obtain fully densified bulk Cu-matrix composites reinforced with 0.8 vol % uniformly distributed RGO nanosheets (see Supporting Information for more details).^{22,23} A pure Cu matrix was also prepared using the same fabrication procedures for comparison purposes. Both of the samples were annealed at 473 K for 20 min before microstructure and mechanical property characterizations. Figure 1a-d reveal the microstructural features of the RGO-Cu composite at multiple length scales. Crystallographic texture was found to be relatively weak in the composite, as revealed by the pole-figure maps obtained by X-ray diffraction (XRD) (Figure 1a). The cross-sectional microstructure of the composite (Figure 1b) indicates a laminated structure with Cu grains elongated along the rolling direction. Transmission electron microscopy (TEM) examinations further revealed that the grain boundaries of the Cu matrix were decorated with RGO nanosheets (Figure 1c) and that no RGO was present in the grain interiors (see Supporting Information for more details, Figure S1). The RGO nanosheets at the grain boundaries were found to contain a few layers (as many as ~10 layers, Figure 1d) with an average interlayer spacing of 0.52 nm and were sandwiched between adjacent Cu grains. Here, the notably greater interlayer spacing than that of pristine graphene (0.34 nm) likely arose from the presence of various residual defects (such as sp³ bonds) in the RGO nanosheets (Figure S2) and from their slightly curved morphology. The sharp Cu/RGO/Cu interface (Figure 1d) suggests no oxidation formation during fabrication, as evidenced also by the synchrotron X-ray diffraction (SXRD) results (Figure S3). Grain size distribution measured from ionchanneling images (using focused ion beam, FIB) and darkfield TEM images consistently show average Cu grain sizes of ~300 and ~130 nm parallel and perpendicular to the lamellar (rolling) directions, respectively. The pure monolithic Cu matrix was found to have a similar grain structure as the RGO-Cu composite (Figure S4), suggesting that the main microstructural difference between these two materials was the constituent of the grain boundary.

Figure 1e shows the uniaxial tensile response of the pure Cu matrix and the RGO-Cu composite, where the tensile direction was parallel to the laminates. Strikingly, the composite shows a yield strength of 557 ± 21 MPa, an ultimate tensile strength of 705 ± 18 MPa, and an engineering elongation-to-failure strain as large as $10.5 \pm 1.3\%$, which are pronouncedly stronger than those of a pure Cu matrix (yield strength 458 ± 20 MPa and ultimate tensile strength 494 ± 21 MPa) and comparable to the total elongations of pure Cu. Notably, the uniform elongation value increases from $1.7 \pm 0.3\%$ to $4.3 \pm 0.5\%$ after

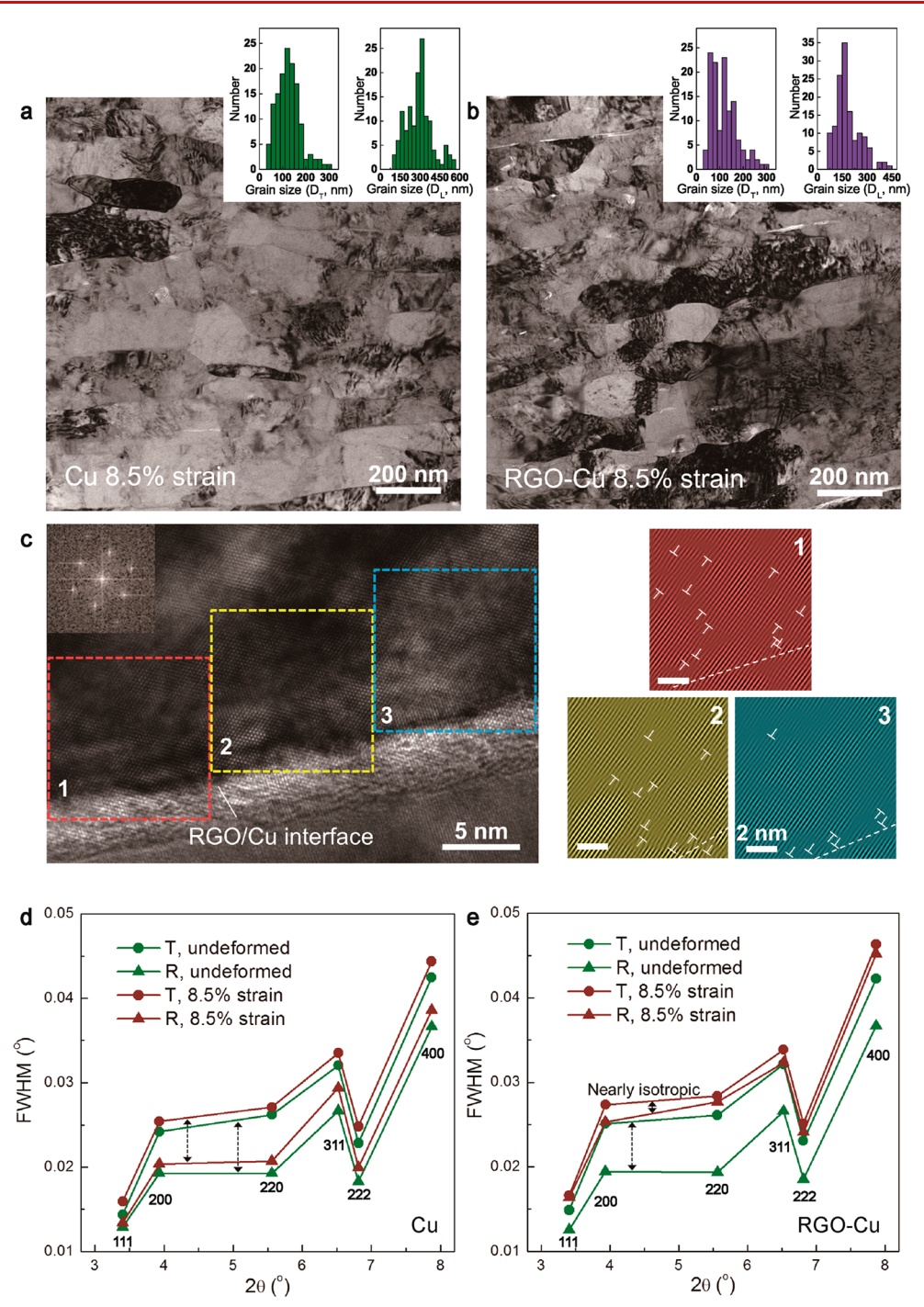


Figure 3. Post-mortem microstructure analysis of pure Cu matrix and RGO-Cu composite. (a, b) Bright-field TEM images of the pure Cu and the RGO-Cu composite, respectively, after 8.5% compressive true strain. The grain sizes parallel and perpendicular to the rolling direction are denoted by D_L and D_T , respectively, and their histograms are measured by dark-field TEM images. (c) High-resolution TEM image taken at the RGO/Cu interface after a compressive true strain of 8.5%. The beam direction is along $\langle 110 \rangle$ axis, as reflected by the fast Fourier transform (FFT) of the Cu matrix (inset). The inverse Fourier-filtered images from the three boxed regions (denoted by 1, 2, and 3) show the presence of a high density of dislocations near the boundary (white dashed line). (d,e) fwhm as a function of the diffraction angle (2θ) before compression and after deformation for the two sample sets, respectively. These data were extracted from the profile fitting of the SXRD spectra, where "R" (rolling) and "T" (transverse) refer to the diffraction directions parallel and perpendicular to the lamellar/rolling direction, respectively (Figure S7). The difference in fwhm magnitude between "R" and "T" orientations are indicated by double-headed arrows.

RGO incorporation. The tensile response of the RGO-Cu composite also shows a substantial improvement in ductility/ uniform elongation over nanograined pure Cu with comparable tensile strength, which usually exhibits premature fracture behavior^{4,14} or highly limited uniform elongation (<3%).^{24,25} The considerable (~22%) increase in the yield

strength of the RGO-Cu composite with only 0.8 vol % RGO concentration compared with the yield strength of pure Cu is attributable to a combined effect of RGO load-sharing and RGO/Cu interfaces acting as stronger barriers for dislocation propagation than Cu grain boundaries.²³

According to Considère's criterion, 26 larger uniform elongation should correlate with a higher strain-hardening capacity, which delays the onset of necking. As demonstrated in Figure 1f, the strain-hardening rate ($\Theta = d\sigma/d\varepsilon$, where σ and ε are the true stress and the true strain, respectively) vs true strain curves demonstrate that the RGO-Cu composite exhibits a higher Θ than its pure Cu counterpart throughout the entire probed strain range, for loading direction perpendicular to the lamellar direction. Here, a compressive, rather than tensile, stress-strain response (Figure 1e) was used because the former is considered to be less sensitive to nanovoids/weak interfaces and is consequently associated with an extended plastic deformation regime in metals and metalbased materials, 11,27 enabling a more precise evaluation of the strain-hardening behavior. The tensile stress-strain curves were shown to produce essentially identical strain-hardening rates to those under compression, using the segment between the yield point and peak stress (Figure S5).

Figure 1g displays a compilation of data reported by various research groups on the compressive strain-hardening rate and yield strength of nano/ultrafine-grained pure Cu, ^{23,28-34} where a distinct trade-off correlation between the two parameters is observed. Remarkably, the trend of the data for the RGO-Cu composite in this study clearly differs from the usual trend. Notably, although high-strength and high-ductility nanostructured Cu has been obtained by introducing nanotwins into the grain interior ¹⁴ and/or through the formation of a bimodal grain structure, ¹² we rarely observe nanotwins in the as-fabricated RGO-Cu composite, where the grain size distribution of the Cu matrix is fairly uniform (Figure S4), suggesting that the high-strength and high-ductility behavior of the RGO-Cu composite cannot be explained from the perspectives of twins or bimodal grain distributions.

We conducted progressive multiple stress-relaxation compressive tests (Figure 2a) to probe the origin of the improved strain-hardening ability of the RGO-Cu composite, from which the dislocation kinetics can also be deduced.³⁵ The applied stress, σ , has two components: $\sigma = \sigma^* + \sigma_w$, where σ^* is the effective stress needed to overcome the short-range barriers and σ_u is the long-range internal stress (athermal stress) that impedes dislocation motion.³⁶ The decrease in relaxation rate at the onset of the holding stage along one series (Figure 2b) at specific true strains (2.5%, 5.5%, and 8.5%) was likely caused by the increasing long-range internal stress during each relaxation segment.³⁶ The evolution of σ_{μ} over successive relaxations can be identified by fitting each stress-relaxation curve (the relevant method for calculating σ_{μ} is given in the Supporting Information). A more intense improvement of long-range internal stress after one relaxation series can be found for the composite, especially at true strains of 5.5% and 8.5% (Figure 2c). After the series at 5.5% strain, σ_{μ} increased by 4.9 and 6.5 MPa for pure Cu and the RGO-Cu composite, respectively. For stress relaxations at 8.5% strain, the change in σ_{μ} after the relaxation series is also higher for the RGO-Cu composite (4.6 MPa) than for the pure Cu matrix (1.5 MPa). The greater increase in σ_{μ} along one relaxation series for the RGO-Cu composite indicates a higher mobile dislocation accumulation rate during deformation, in correlation with the higher strain-hardening rate. 36,37

The physical activation volume (V^*) of the average dislocation velocity can be determined from multicycle relaxation tests,³⁸ which is a critical parameter indicative of the operating plastic deformation mechanism, reflecting the

combined effect of dislocation density-based deformation in the grain interior and the resistance to dislocation motion rendered by obstacles (grain boundaries in this study).³⁹ Figure 2d presents V^* for the pure Cu matrix and the RGO-Cu composite as a function of the strain at which the relaxation was done. A monotonic decrease in V^* with increasing strain can be observed for the composite, while the change in V^* for the pure Cu matrix was shown to flatten out after 2.5% strain (the method for V^* calculation can be found in the Supporting Information). This decreasing trend in activation volume of the RGO-Cu composite suggests that the defect density increases with increasing strain, which makes dislocation initiation/propagation more difficult; i.e., strain hardening occurs. Notably, the RGO-Cu composite has activation volumes consistently smaller than those of the pure Cu matrix at various strain levels; this difference originates from the combined effect of enhanced dislocation obstructions at grain boundaries and the presence of stronger defect accumulations during straining.²³

Interpretation of the improved strain-hardening capacity of the RGO-Cu composite over that of pure Cu relies on an understanding of the different processes that govern plastic deformation and dislocation accumulation. TEM analysis of the postcompression ($\varepsilon = 8.5\%$) pure Cu matrix revealed a nearly identical microstructure to that of the as-fabricated sample; the grain size distribution was essentially unchanged (Figure 3a), and no apparent increase in twin density was found, indicating a low dislocation/defect storage capacity in pure Cu. In general, in the nanograined regime (grain size \approx 100 nm), the intragranular dislocation sources would cease to dominate the deformation process, and grain-boundary-assisted dislocation nucleation would begin. ¹³ The important role played by grain-boundary-mediated dislocation emission/ adsorption in the pure Cu matrix can be appreciated by the dislocation kinetics. The physical activation volume of the pure Cu matrix was calculated to be $27b^3$ at $\varepsilon = 2.5\%$ and was further reduced with increasing strain (Figure 2d), becoming substantially smaller than the value corresponding to the intragranular dislocation interaction (cutting dislocation forests) mechanism, which usually ranges from 100 to $1000b^{3.38}$ and falls in the same range of interfacial plasticity governed deformation mechanism (12-44b3).40-42 In other words, dislocations nucleated from one grain boundary tended to slip through the whole grain and adsorbed onto the grain boundary on the other side, with limited chance to interact with other dislocations in the grain interior, whose mechanism has been well established from in situ TEM straining experiment and computer simulations conducted on various nanostructured metals. ^{3,10,13} In addition, in the deformed pure Cu matrix in this study, the absence of dislocation pile-ups observed from the post-mortem TEM microstructural characterization (Figure S6) clearly suggests the depletion of dislocations near the grain boundaries. The same mechanism is also observed in bicrystalline metal nanopillars with similar grain sizes, where the grain boundary vicinities are found to be free of defect/dislocation agglomerates. 43,44 Therefore, in a pure Cu matrix, strain-induced dislocations became quickly saturated upon deformation, and additional straining did not render further hardening because of the dynamic balance between the generation of dislocations and their recovery.

However, this is not the case for the RGO-Cu composite. In particular, we found that the initially elongated Cu grains became significantly shortened after the composite was loaded

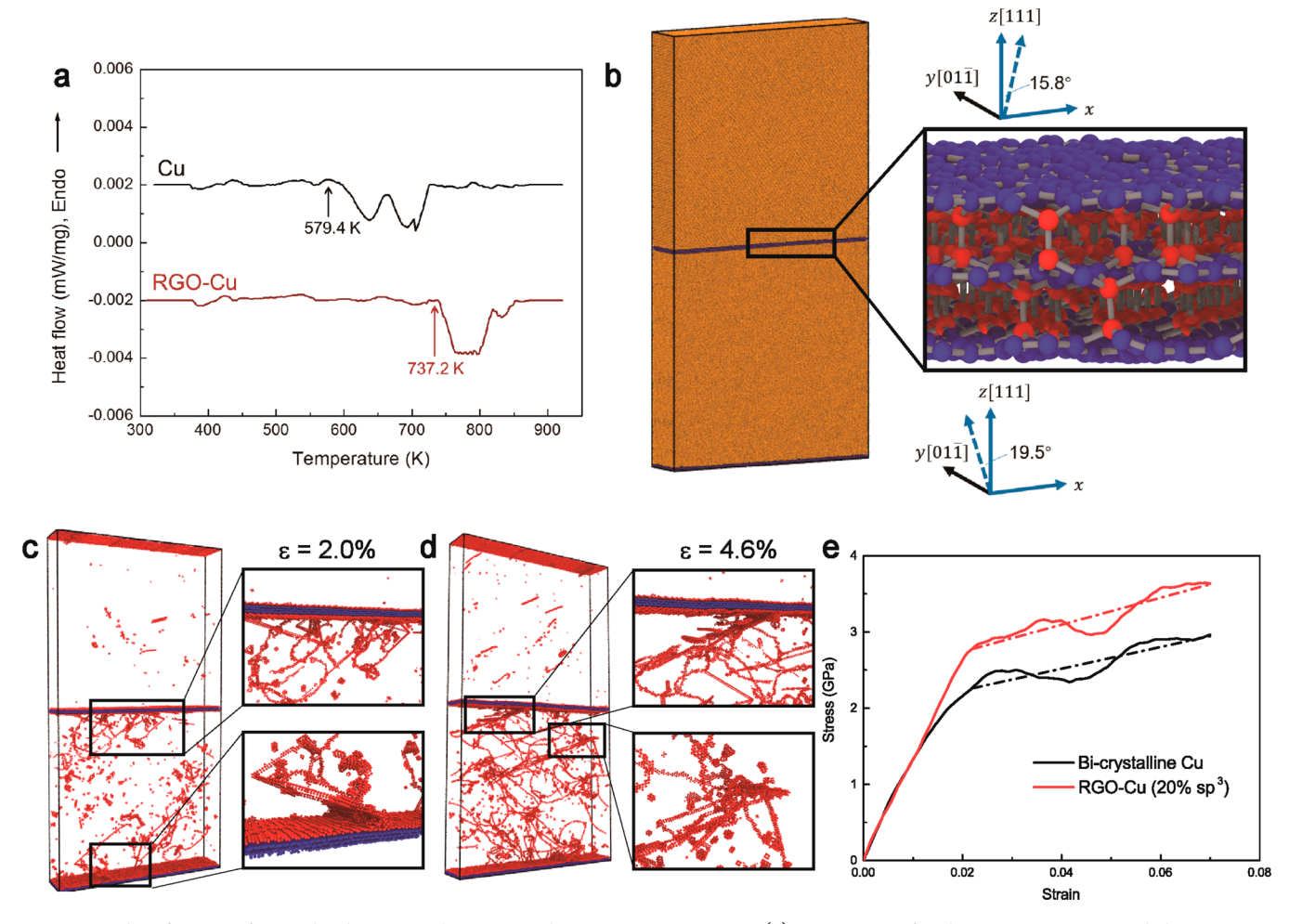


Figure 4. Identification of strain-hardening mechanisms in the RGO-Cu composite. (a) DSC curves for the pure Cu matrix and the RGO-Cu composite at a heating rate of 4 K/min to a maximum temperature of 923 K. (b) Atomic configurations of the Cu-RGO-Cu system used in MD simulations. Three layers of graphene with sp³-hybridized bond concentration of 20% were sandwiched between two Cu slabs. Atoms with sp² bonds are painted in blue, while atoms with sp³ bonds are painted in red. (c,d) Typical snapshots of deformed samples at 2.0% and 4.6% tensile strains, respectively. Numerous dislocations piled up near grain boundaries, and some dislocations tangled, leading to enhanced capacity of dislocation storage. (e) Stress—strain curves from MD simulations of the pure bicrystalline Cu and the RGO-Cu composites. Curves at the 2–7% strain range were fitted by dashed straight lines to calculate the strain-hardening rates.

with a compressive strain of 8.5%, with the grain size parallel to the rolling direction reduced to ~150 nm, demonstrating a nearly equiaxed grain structure (Figure 3b). This grain fragmentation mechanism was previously considered to operate only at a grain size of at least a few hundred nanometers for monolithic metals deformed at low strain rates and at room temperature. 13 Thus, compared to the similar preand post-deformation microstructures of the pure Cu matrix, the pronounced grain refinement in the deformed RGO-Cu composite unambiguously suggested that evident dislocation storage was rejuvenated by the RGO incorporation at the Cu grain boundaries. Furthermore, we found a high density of dislocations near the grain boundaries in the postcompression composite (Figure 3c), in stark contrast to the absence of massive dislocation pile-ups in the deformed pure Cu matrix (Figure S6). The aforementioned post-mortem TEM microstructural characterization confirms that dislocation trapping and storage in the RGO-Cu composite was profound, which most likely contributed to the enhanced strain-hardening

Figure 3d,e show the *ex situ* SXRD peak-broadening results as a function of the diffraction angle (2θ) for the pure Cu

matrix and the RGO-Cu composite before and after being compressed by 8.5% of strain, where peak broadening was quantified using the full width at half-maximum (fwhm) of each diffraction peak. The diffraction patterns and data are provided in the Supporting Information (Figure S7 and Table S1). In addition to offering a more precise statistical approach for bulk materials, these SXRD measurements can resolve the crystallographic anisotropy of the specimen because the attached two-dimensional detector can record X-ray signals scattered from different angles on a single diffraction pattern (Figure S7a). 45 SXRD peak broadening is generally believed to be associated with the presence of grain boundaries and dislocations, which are either statistically stored or geometrically necessary as a result of deformation heterogeneity. Considering the large number of dislocation slip systems in face-centered cubic (fcc) metals and the presence of a weak texture in both the pure Cu matrix and the RGO-Cu composite, the fwhm anisotropy induced by dislocation distribution can be neglected, and the dominant source for peak-broadening anisotropy is the nonequiaxed grain morphology. In the as-fabricated state (the green data points in Figure 3d,e), a clear anisotropy in the grain structure was observed in

both the pure Cu matrix and the RGO-Cu composite, where the fwhm values in the rolling direction (R, parallel to the laminate) are substantially smaller than those in the transverse direction (*T*, perpendicular to the laminate). This observation suggests an elongated grain morphology with a larger in-plane (rolling direction) average grain size than out-of-plane (transverse direction) average grain size, consistent with the results of the TEM and ion-channeling imaging characterizations (Figures 1b and S4). After the specimens underwent a compressive strain of 8.5%, however, the peak broadening of the two sample sets showed very distinct evolutions. In the case of the pure Cu matrix (Figure 3d, red data points), although a moderate increase in fwhm for all diffraction peaks was observed in both the rolling and transverse directions, the relative difference in fwhm between the two orientations before and after deformation remained similar (as indicated by the black arrows), indicating that the anisotropic grain structure was retained. However, the peak broadening in the rolling direction in the composite increased drastically after deformation so that the fwhm of the rolling and transverse directions became similar (Figure 3e, red data points), a strong evidence for a fairly isotropic grain structure. The peakbroadening magnitude scales with defect density (in our case, grain boundaries and dislocations); thus, these results implied a considerable increase in the number of grain boundaries and/ or a substantial buildup of dislocations in the post-compression composite, as interpreted from TEM observations (Figure 3b,c).

At a constant temperature and strain rate, the dislocation kinetics is determined by the microstructure of the material being tested. In contrast to the pure Cu matrix, the RGO-Cu composite has higher and increasing long-range internal stresses and lower and decreasing physical activation volumes upon deformation (Figure 2c,d). Meanwhile, the composite showed a conversion from strong anisotropy to an essentially isotropic grain structure (Figure 3b,e). These observations were consistent with the improved strain-hardening capacity of the composite (Figure 1e,f), and the massive dislocation accumulation and grain refinement observed in postdeformation microstructural analysis (Figures 3b,c,e), all of which unanimously suggested a highly stabilized grainboundary structure as a result of RGO inclusion. By employing differential scanning calorimetry (DSC) measurements (Figure 4a), we measured the grain-boundary energy of the RGO-Cu composite to be $0.56 \pm 0.08 \text{ J/m}^2$, ~35% lower than that of the pure Cu matrix $(0.86 \pm 0.07 \text{ J/m}^2)$ (see Supporting Information for details of measurement). This value (0.86 J/ m²) fell into the range reported for the boundary energy of typical incoherent interfaces $(0.8-2.5 \text{ J/m}^2)^7$ and was also consistent with theoretical studies on the grain-boundary energy of pure Cu. 46 The reduced grain-boundary energy of the RGO-Cu composite also led to improved thermal stability; the onset temperature for grain growth increased from 579.4 K for the pure Cu matrix to 737.2 K for the RGO-Cu composite (Figure 4a), although the drag effect of RGO could impede grain-boundary migration and thus may also contribute to that

The simultaneous improvement in strength and ductility in the RGO-Cu composite was achieved by taking advantage of the following two factors. First, for the yield strength, the graphene nanosheets sandwiched at the grain boundaries serve as barriers for dislocation slip or transmission. The grainboundary characteristics are likely to be similar in both fine and coarse grains, as revealed by computer simulations, 47 which give a unified Hall-Petch strengthening contribution ($\Delta \sigma$ = $kd^{-1/2}$) applicable for metals with various grain sizes down to the nanograined regime.³⁹ The change in the grain-boundary strengthening magnitude owing to the nanofiller incorporation is embedded in the increased coefficient k, whose influence would become more pronounced with decreasing grain size. It was demonstrated that the threshold stress for dislocations penetrating the grain boundaries increased by almost 16 times after RGO incorporation, and the associated coefficient k in the Hall-Petch relation increased to ~4 times that of pure Cu. 23 This greatly elevated grain-boundary strengthening contribution, together with the load-bearing effect of RGO during tensile testing (the strength of RGO used in this work was calculated to be ~2.8 GPa, see Supporting Information for more details), is beneficial for improving the yield strength of the RGO-Cu composite. The strengthening contributions from the enhanced grain boundary strengthening and from the RGO load-bearing to the overall yield strength increment were estimated to be 78% and 22%, respectively (see Supporting Information for more details), clearly suggesting that the nanofiller-induced enhancement in boundary-strengthening is the governing mechanism accounting for the high strength of nanolaminated RGO-Cu composites.

Second, for the strain-hardening capacity, by virtue of RGO inclusion at the grain boundaries, the decrease in grainboundary energy provided sufficient room for dislocation storage in the grain interiors and at grain boundaries during deformation. In particular, the reduced grain-boundary energy in the composite lowered the thermodynamic driving force for dislocation annihilation/recovery at the boundaries (see Supporting Information for more discussion), and dislocations then interacted with each other and accumulated near the grain boundaries or in the matrix grain interiors to form substructures that eventually led to grain fragmentation (Figure 3b). This process produced an increasing long-range internal stress that resisted further plastic deformation and thereby contributed to strain hardening. Such "dynamic" Hall-Petch strengthening is analogous to other mechanisms that particularly promote strain hardening, e.g., transformation⁴⁸ or twinning-induced plasticity mechanisms, 49-51 both of which rely on the basic principle of providing additional strengthening sources during deformation through the creation of new interfaces. The tailoring of dislocation kinetics by grainboundary/interface engineering has also recently been demonstrated by in situ TEM studies, where dislocation annihilation in a Cu-Au alloy was considerably mitigated by the introduction of an interface.⁵²

To complement the experiments and reveal the underlying deformation mechanisms, we performed large-scale molecular dynamics (MD) simulations to explore the interfacial features and deformation behaviors of the RGO-Cu composite. Figure 4b shows the atomic configuration of RGO-Cu used in MD simulation. Three-layer graphene with an sp³ bond concentration of 20% (similar to value determined from X- analysis, Figure S2) was sandwiched between two Cu slabs, which is similar to the experimentally observed structures. We first calculated the interfacial energies of the RGO-Cu composite and the pure bicrystalline Cu. The energies for the RGO-Cu composite and pure bicrystalline Cu were as high as 0.61 and 0.80 J/m², respectively, in good agreement with experimental measurements (0.56 \pm 0.08 J/m² for the RGO-Cu composite and 0.86 \pm 0.07 J/m² for the pure polycrystalline Cu). This

result verified the decrease in interfacial energy due to the introduction of RGO on grain boundaries and also indicated that such decrease mainly arose from the van der Waals interactions between the RGO and the Cu (the method used to calculate the interfacial energy is supplied in the Supporting Information).

We further mimicked the uniaxial tension for the bicrystalline Cu and the RGO-Cu composite along the x axis (Figure 4b) and investigated their deformation behaviors. To study the hardening behaviors, the initial simulated samples were set to contain pre-existing defects, including dislocations, stacking faults, and vacancies, which were similar to those in experimental samples. More details about the MD simulations are given in the Supporting Information. Figure 4c,d captures two snapshots of stretched RGO-Cu composite at 2.0% and 4.6% strains, respectively. In the initial stage of plastic deformation, the dislocation pile-up occurred near the RGO/ Cu interfaces, as evidenced by Figure 4c. With further deformation, more dislocations were pinned near the interfaces, and some nucleated dislocations interact with each other or with pre-existing dislocations, leading to the formation of abundant dislocation tangles in the grain interior (Figure 4d), closely matching the experimental observations (Figures 3b,c). These dislocation tangles and pile-up dislocations blocked further motion of other dislocations, leading to substantial hardening. These mechanistic details reflect the good dislocation storage capacity of the RGO-Cu composite by dislocation pile-up or entanglement. For pure Cu with the same grain size, however, dislocations were found to nucleate from one grain boundary and then slip through the whole grain with little hindrance and were finally absorbed at the opposite grain boundary (as shown in Figure S8), and no dislocation pile-up at grain boundaries was clearly observed.

Figure 4e shows simulated stress-strain curves for the bicrystalline Cu and the RGO-Cu composite. Notably, the RGO-composite composite exhibits a critical strain of approximately 2.0%, where plastic deformation is initiated; this strain value is larger than the corresponding value for the bicrystalline Cu (~1.2%). This phenomenon is attributed to the initiation of plastic deformation beings dominated by dislocation nucleation/emission from the grain boundaries/ interfaces (Movie S1), which was harder to operate in the RGO-Cu composite due to grain-boundary stabilization. After the linear elastic regime, the RGO-Cu composite had a higher stress level and more significant strain hardening than the bicrystalline Cu. We calculated the strain-hardening rates by linearly fitting the 2% to 7% strain segment of the stress-strain curves (Figure 4e), and found an almost 25% increase in the strain-hardening rate for the RGO-Cu composite over that of the bicrystalline Cu. This observation is consistent with the experimental measurements shown in Figure 1e,f. To some extent, it implies that the RGO-Cu composite exhibited enhanced dislocation storage capability compared with bicrystalline Cu. Notably, the simulated samples exhibited higher yield strengths than the experimental results, which is attributed to distinct differences in the spacing of lamellar Cu, strain rate, and initial defect structure between MD simulations and experiments. Despite these differences, our MD simulations not only revealed the microstructural evolution and underlying deformation mechanisms but also provided mechanistic insights into the strengthening and hardening behavior of the RGO-Cu composite.

Figure S9 shows the atomic von Mises shear strain contours of simulated RGO-Cu composite at different tensile strains. It indicates that there exists a distinct strain incompatibility between RGO and Cu matrix during deformation of RGO-Cu composite. Such strain incompatibility facilitates the generation of strain gradient in RGO-Cu composite and the formation of a high density of geometrically necessary dislocations (GNDs), 53,54 which lead to the dislocation pileups in the vicinity of the grain boundary (Figure 3c) and to some extent suppress the dislocation transportation across the RGO/Cu interface, potentially responsible for both strain hardening and grain refinement observed in the deformed RGO-Cu composite. Although the GND-induced strain hardening has been observed in polycrystalline metals with grain sizes ranging from several hundreds of nanometers to micrometers, 55 experimental evidence of GND generation in smaller grains (<100 nm or so) remains controversial.⁵⁶ To assess the net role played by nonuniform deformation in strain hardening, we processed a set of RGO-Cu composite samples via further cold rolling (thickness reduction ~10%) to consume the dislocation storage capacity. Subsequent compressive tests showed that the extra strain-hardening ability of the cold-rolled composite almost disappeared (Figure S10). The absence of the additional strain hardening of the reprocessed RGO-Cu composite inferred a relatively weak influence of strain heterogeneity between the RGO and the Cu matrix in promoting the strain-hardening capacity of the composite, in comparison with the effect of the reduced grainboundary energy. Furthermore, our experimental and simulation results showed that the RGO-Cu composites have higher strain hardening capacity than the individual Cu counterparts. Our simulations also showed that the RGO nanosheet exhibited a brittle fracture with the fracture strain of about 8% (Figure S11), which is comparable to that of RGO-Cu composite in our experiments (about 10%). It implies that when the RGO-Cu composites failed, the RGO nanosheets in the composite might have only underwent the elastic deformation and been stretched to fracture. Therefore, it is emphasized that high strain hardening capacity of RGO-Cu composite mainly originates from the incorporation of nanofillers into grain boundaries of Cu matrix and the resultant reduction in grain boundary energy, as demonstrated by our experiments and atomistic simulations.

This work distinguishes itself from the previous studies on graphene-metal composites by emphasizing the role played by grain boundary engineering in regaining the strain hardening capacity of nanostructured metals. This extra dislocation storage mechanism is believed to be the result of the considerable volume fraction of grain boundaries and their vicinities, which significantly promote dislocation-interface interactions. Compared to existing literature reporting dislocation obstruction by graphene/metal interfaces, the strengthening and toughening of metals by grain-boundary engineering found in this work extends our understanding on nanofiller-reinforced metal matrix composites: incorporating extrinsic nanofillers (graphene) at the grain boundaries of nanostructured metals would not only enhance the strong dislocation hindrance at the boundaries but would also promote dislocation storage ability in the grain interior of the metal matrix, potentially making the nanostructured metals both strong and ductile.

In summary, using the RGO-Cu model material, we have shown that incorporation of RGO nanofillers into grain

boundaries led to a more than 30% decrease in the grainboundary energy and subsequently a striking improvement in both strength and uniform elongation over pure Cu. Our results clearly demonstrated the unique role of RGO nanofillers in strengthening and hardening of RGO-Cu composites, as well as the importance of reduced grainboundary energy in facilitating dislocation storage and strainhardening capacity in nanostructured Cu. The novel grainboundary energy engineering approach by nanofillers reported in this work reveals the significance of nanofillers in modulating dislocation activity and subsequently the plastic deformation mechanism of the nanostructured metals. rendering the mechanical property well exceeds that predicted by the "rule-of-mixtures". Given the availability of nanofillers of various types, defect states, and intrinsic properties, as well as the relatively simple fabrication strategy of using conventional metal processing techniques, we believe that the novel concept of nanofiller-metal composites can be readily extended to other materials systems, leading to comprehensive enhancement of the mechanical properties of nano/ultrafine-grained metals and to mitigation of the strength-ductility trade-off.

Further reduction of the grain size down to the sub-100 nm regime would be exciting, although technically challenging, as the governing deformation mechanism of monolithic metals with such small grain size would gradually switch from conventional dislocation-accommodated mechanisms to grain boundary dominated processes. In this regard, the reduced grain-boundary energy may delay such a mechanism transition and particularly, the softening as a result of the grain boundary dominated behavior, eventually rendering metals with ultrahigh strength and strain hardening capacity (tensile ductility).

ASSOCIATED CONTENT

S Supporting Information

The Supporting Information is available free of charge on the ACS Publications website at DOI: 10.1021/acs.nanolett.8b02375.

Details on experimental methods; sample characterization and tensile/compressive testing; multiple compressive stress—relaxation tests; calculation of long-range internal stress (σ_{μ}) and physical activation volume (V^*); calculation of grain-boundary/interface energy by DSC analysis; atomistic simulations; Table S1 and Figure S1—S12 (PDF)

Movie of atomistic simulation of uniaxial tension of RGO-Cu composite (AVI)

AUTHOR INFORMATION

Corresponding Authors

*E-mail: guoq@sjtu.edu.cn.

*E-mail: xiaoyanlithu@tsinghua.edu.cn.

*E-mail: zhangdi@sjtu.edu.cn. Tel: +86-21-34202634. Fax: +86-21-34202749.

ORCID

Qiang Guo: 0000-0001-9590-4413

Author Contributions

^{||}Z.L. and H.W. contributed equally to this work.

Notes

The authors declare no competing financial interest.

ACKNOWLEDGMENTS

The authors would like to acknowledge the financial support from the Ministry of Science and Technology of China through the National Key R&D Plan (Grant Nos. 2016YFE0130200, 2017YFB0703103); the National Natural Science Foundation of China (Grant Nos. 51801120, 51771111, 51771110, 51671130, 51501111, 11522218), and the Science & Technology Committee of Shanghai Municipality (Grant No. 17520712400). H.G. acknowledges financial support from the U.S. National Science Foundation (Grant No. DMR-1709318). Dr. Thomas Voisin in Lawrence Livermore National Laboratory is acknowledged for doing SXRD experiments at the Advanced Photon Source (APS) of Argonne National Laboratory at beamline 6-ID-D. The simulations were performed on the TianHe-1 supercomputer at the National Supercomputer Center in Tianjin.

REFERENCES

- (1) Hall, E. O. Proc. Phys. Soc., London, Sect. B 1951, 64, 747-753.
- (2) Petch, N. J. J. Iron Steel Inst. 1953, 174, 25-28.
- (3) Kumar, K. S.; Van Swygenhoven, H.; Suresh, S. Acta Mater. **2003**, *51*, 5743–5774.
- (4) Wang, Y. M.; Wang, K.; Pan, D.; Lu, K.; Hemker, K. J.; Ma, E. Scr. Mater. 2003, 48, 1581–1586.
- (5) Liddicoat, P. V.; Liao, X. Z.; Zhao, Y.; Zhu, Y.; Murashkin, M. Y.; Lavernia, E. J.; Valiev, R. Z.; Ringer, S. P. *Nat. Commun.* **2010**, *1*, 63.
- (6) Lu, K.; Lu, L.; Suresh, S. Science 2009, 324, 349-352.
- (7) Lu, K. Nat. Rev. Mater. 2016, 1, 16019.
- (8) Udler, D.; Seidman, D. N. Phys. Rev. B: Condens. Matter Mater. Phys. 1996, 54, R11133-R11136.
- (9) Budrovic, Z.; Van Swygenhoven, H.; Derlet, P. M.; Petegem, S. V.; Schmitt, B. *Science* **2004**, *304*, 273–276.
- (10) Yamakov, V.; Wolf, D.; Phillpot, S. R.; Mukherjee, A. K.; Gleiter, H. Nat. Mater. **2004**, *3*, 43–47.
- (11) Wang, Y. M.; Ma, E. Acta Mater. 2004, 52, 1699-1709.
- (12) Wang, Y. M.; Chen, M. W.; Zhou, F. H.; Ma, E. Nature 2002,
- (13) Meyers, M. A.; Mishra, A.; Benson, D. J. Prog. Mater. Sci. 2006, 51, 427–556.
- (14) Lu, L.; Shen, Y. F.; Chen, X. H.; Qian, L. H.; Lu, K. Science **2004**, 304, 422-426.
- (15) Liu, X. C.; Zhang, H. W.; Lu, K. Science 2013, 342, 337-340.
- (16) Wang, Y. M.; Voisin, T.; McKeown, J. T.; Ye, J.; Calta, N. P.; Li, Z.; Zeng, Z.; Zhang, Y.; Chen, W.; Roehling, T. T.; Ott, R. T.; Santala, M. K.; Depond, P. J.; Matthews, M. J.; Hamza, A. V.; Zhu, T. *Nat. Mater.* **2018**, *17*, 63–71.
- (17) Van Swygenhoven, H.; Derlet, P. M.; Frøseth, A. G. Nat. Mater. **2004**, *3*, 399–403.
- (18) Jiang, L.; Wen, H.; Yang, H.; Hu, T.; Topping, T.; Zhang, D.; Laverialia, E. J.; Schoenung, J. M. Acta Mater. 2015, 89, 327–343.
- (19) Tjong, S. C. Mater. Sci. Eng., R 2013, 74, 281-350.
- (20) Bakshi, S. R.; Lahiri, D.; Agarwal, A. Int. Mater. Rev. 2010, 55, 41–64.
- (21) Chen, L. Y.; Xu, J. Q.; Choi, H.; Pozuelo, M.; Ma, X.; Bhowmick, S.; Yang, J. M.; Mathaudhu, S.; Li, X. C. *Nature* **2015**, 528, 539–543.
- (22) Li, Z.; Guo, Q.; Li, Z. Q.; Fan, G.; Xiong, D. B.; Su, Y.; Zhang, J.; Zhang, D. *Nano Lett.* **2015**, *15*, 8077–8083.
- (23) Li, Z.; Zhao, L.; Guo, Q.; Li, Z. Q.; Fan, G.; Guo, C.; Zhang, D. Scr. Mater. **2017**, 131, 67–71.
- (24) Wang, Y. M.; Sansoz, F.; Lagrange, T.; Ott, R. T.; Marian, J.; Barbee, T. W., Jr; Hamza, A. V. *Nat. Mater.* **2013**, *12*, 697–702.
- (25) Lu, L.; Chen, X.; Huang, X.; Lu, K. Science **2009**, 323, 607–610
- (26) Hart, E. W. Acta Metall. 1967, 15, 351-355.

(27) Kim, Y.; Lee, J.; Yeom, M. S.; Shin, J. W.; Kim, H.; Cui, Y.; Kysar, J. W.; Hone, J.; Jung, Y.; Jeon, S.; Han, S. M. *Nat. Commun.* **2013**, *4*, 2114.

- (28) Farrokh, B.; Khan, A. S. Int. J. Plast. 2009, 25, 715-732.
- (29) Khan, A. S.; Farrokh, B.; Takacs, L. J. Mater. Sci. 2008, 43, 3305-3313.
- (30) Valiev, R. Z. Mater. Sci. Eng., A 1997, 234-236, 59-66.
- (31) Dalla Torre, F. H.; Pereloma, E. V.; Davies, C. H. Acta Mater. **2006**, *54*, 1135–1146.
- (32) Jia, D.; Ramesh, K. T.; Ma, E.; Lu, L.; Lu, K. Scr. Mater. 2001, 45, 613–620.
- (33) Wang, Y. M.; Ma, E. Mater. Sci. Eng., A 2004, 375-377, 46-52.
- (34) Suryanarayanan Iyer, R.; Frey, C. A.; Sastry, S. M.; Waller, B. E.; Buhro, W. E. *Mater. Sci. Eng., A* **1999**, 264, 210–214.
- (35) Wu, X. L.; Jiang, P.; Chen, L.; Yuan, F. P.; Zhu, Y. T. Proc. Natl. Acad. Sci. U. S. A. **2014**, 111, 7197–7201.
- (36) Caillard, D.; Martin, J. L. Thermally Activated Mechanisms in Crystal Plasticity; Pergamon: Amsterdam, 2003.
- (37) Meyers, M. A. Mechanical Metallurgy Principles and Applications; Prentice-Hall: NI, 1984.
- (38) Wang, Y. M.; Hamza, A. V.; Ma, E. Acta Mater. 2006, 54, 2715-2726.
- (39) Li, J. C. M. Mechanical Properties of Nanocrystalline Materials; Pan Stanford Publishing: Singapore, 2011.
- (40) Lu, L.; Zhu, T.; Shen, Y.; Dao, M.; Lu, K.; Suresh, S. Acta Mater. 2009, 57, 5165-5173.
- (41) Asaro, R. J.; Suresh, S. Acta Mater. 2005, 53, 3369-3382.
- (42) Zhu, T.; Li, J.; Samanta, A.; Kim, H. G.; Suresh, S. Proc. Natl. Acad. Sci. U. S. A. 2007, 104, 3031–3036.
- (43) Kunz, A.; Pathak, S.; Greer, J. R. Acta Mater. 2011, 59, 4416–4424.
- (44) Kim, Y.; Lee, S.; Jeon, J. B.; Kim, Y. J.; Lee, B. J.; Oh, S. H.; Han, S. M. Scr. Mater. **2015**, 107, 5–9.
- (45) Lohmiller, J. Investigation of Deformation Mechanisms in Nanocrystalline Metals and Alloys by in Situ Synchrotron X-ray Diffraction; KIT Scientific Publishing: Karlsruhe, 2013.
- (46) Tschopp, M. A.; Mcdowell, D. L. Philos. Mag. 2007, 87, 3871–3892.
- (47) Van Swygenhoven, H. Phys. Rev. B: Condens. Matter Mater. Phys. 2000, 62, 831.
- (48) Li, Z. M.; Pradeep, K. G.; Deng, Y.; Raabe, D.; Tasan, C. C. *Nature* **2016**, 534, 227–230.
- (49) Bouaziz, O.; Allain, S.; Scott, C. Scr. Mater. 2008, 58, 484-487.
- (50) Wei, Y.; Li, Y.; Zhu, L.; Liu, Y.; Lei, X.; Wang, G.; Wu, Y.; Mi, Z.; Liu, J.; Wang, H.; Gao, H. Nat. Commun. 2014, 5, 3580.
- (51) Narayanan, S.; Cheng, G.; Zeng, Z.; Zhu, Y.; Zhu, T. Nano Lett. 2015, 15, 4037-4044.
- (52) Zou, L. F.; Yang, C.; Lei, Y.; Zakharov, D.; Wiezorek, J. M. K.; Su, D.; Yin, Q.; Li, J.; Liu, Z.; Stach, E. A.; Yang, J. C.; Qi, L.; Wang, G.; Zhou, G. Nat. Mater. **2018**, *17*, 56–63.
- (53) Ashby, M. F. Philos. Mag. 1970, 21, 399-424.
- (54) Ma, Z. W.; Ren, Y.; Li, R.; Wang, Y. D.; Zhou, L.; Wu, X.; Wei, Y.; Gao, H. Mater. Sci. Eng., A 2018, 712, 358-364.
- (55) Wu, X. L.; Zhu, Y. T. Mater. Res. Lett. 2017, 5, 527-532.
- (56) Vogt, R.; Zhang, Z.; Li, Y.; Bonds, M.; Browning, N. D.; Lavernia, E. J.; Schoenung, J. M. Scr. Mater. **2009**, *61*, 1052–1055.